Asymmetric magnetic anomalies over young impact craters on Mercury

Asymmetric magnetic anomalies over young impact craters on Mercury

V. Galluzzi[1], J. S. Oliveira[2,3], J. Wright[4], D. A. Rothery[4], and L. L. Hood[5]

[1]INAF, Istituto di Astrofisica e Planetologia Spaziali, Rome, Italy

[2]ESA/ESTEC, SCI-S, Noordwijk, Netherlands

[3]Space Magnetism Area, Payloads & Space Sciences Department, INTA, Torrejón de Ardoz, Spain

[4]School of Physical Sciences, The Open University, Milton Keynes, UK

[5]Lunar and Planetary Laboratory, University of Arizona, Tucson AZ, USA

Corresponding author: Valentina Galluzzi (valentina.galluzzi@inaf.it)

Key Points:

- Stieglitz and Rustaveli are two young impact craters on Mercury associated with overlapping crustal magnetic anomalies.
- The magnetic anomalies are asymmetrical with respect to each crater's center and correlate well with the location of impact melt.
- The impact melt located downrange contains impactor magnetic-carriers that recorded the magnetic field of Mercury at the time of quenching.

Abstract

Mercury's crustal magnetic field map includes anomalies that are related to impact craters. Mercury's surface has a low iron abundance, but it is likely that some impactors brought magnetic carriers able to register the planet's magnetic field that was present during impact. Anomalies associated with the relatively young Rustaveli and Stieglitz craters are asymmetric with respect to the crater center. We analyze the location of the magnetic anomalies and the impact crater morphologies to understand whether there is any correlation. We investigate the geological framework of these two craters to constrain the overall impact dynamics. In both cases, magnetic anomalies correlate well with the location of impact melt and the inferred impact direction. Both impact angles were probably 40–45°, with preferential distribution of the melt downrange. Inversion dipoles suggest that the impact melt located downrange encompasses some magnetized material, which is hence likely responsible for the detected magnetic anomalies.

Plain Language Summary

We observe strong crustal magnetic field imprints near two recent craters on Mercury. We know that the crust of rocky planets may include magnetic elements like iron that can record the local magnetic field under certain circumstances. However, Mercury's crust is known to be remarkably poor in iron. In this study we want to find out whether these observed magnetic imprints near craters happened by chance or if it can be explained by the impactors bringing iron to Mercury's surface. We make a joint-study of two different scientific areas: geology and geophysics. Via the geological study, we found an uneven distribution of 'impact melt', which is material flung out of the crater in molten form during the impact that made the crater. Via the geophysical study, we found evidence that magnetized material correlates with the position of those pools that are found in the downrange direction of the impact. In conclusion, this study supports the hypothesis that iron was brought on Mercury by the impactors.

1 Introduction

The low-altitude campaign (< 120 km) of the NASA MErcury Surface, Space ENvironment, GEochemistry, and Ranging (MESSENGER) mission was fundamental for detecting magnetic field signatures of crustal origin on Mercury (Johnson et al., 2015). However, constraints on the orbit imposed by Mercury's hostile environment allowed these measurements only in a short latitudinal range, between 35°N and 75°N. Maps of the crustal magnetic field at 40 km altitude (Hood, 2016; Hood et al., 2018) show that most of the surface is scarcely magnetized, but with some magnetic anomalies heterogeneously distributed over the surface of the planet. These anomalies do not seem to be related to any specific geological features, except for a few cases where the anomalies are found to be related to basins or craters (Hood et al., 2018, Oliveira et al., 2019a). For example, the strongest signal of the Hermean crustal magnetic field is detected over the Caloris basin, and has an intensity of about 9.5 nT at 40 km altitude

(Hood, 2016), which is comparable to, or somewhat larger than the strongest lunar crustal anomaly intensities (e.g., Richmond and Hood, 2008).

The composition of the magnetic anomalies sources are poorly understood, particularly given that spectroscopic observations have revealed that Mercury's surface is poor in iron (Izenberg et al., 2015; Weider et al., 2014), which would be the best magnetic carrier to record magnetic fields. Understanding their origin is important, because a thermoremanently magnetized body probably holds information about the past core field, which allows understanding of the dynamo evolution, and consequently Mercury's history.

For the Moon, Wieczorek et al. (2012) proposed that impactors could deliver magnetic carriers to the surface, and that in the presence of a core magnetic field this material would become magnetized. This hypothesis was recently suggested for Mercury as well (Hood et al., 2018). This process would result in some craters that are related to anomalies and others that are not, depending on the impactor composition. The eventual distribution of the impactor material depends on several variables: velocity, angle and composition of the impactor, and composition of the surface (Wieczorek et al., 2012). Most of Mercury's original crust has been volcanically resurfaced (e.g., Thomas and Rothery, 2019). Most iron-enriched impact melt and ejecta from basins such as Caloris are likely to lie beneath these flows, rather than at the surface. General correlative studies of magnetic field intensity versus surface composition and geology may therefore not be successful in positively identifying magnetic anomaly source materials.

Here we test the impactor delivery hypothesis by investigating some anomalies that are related, but asymmetrical, with respect to young craters. Inferring the craters impact geometries from geological indicators will help understanding whether the off-centered anomalies are related to the impactor-delivered materials or not.

1.1 Geological Context

The area between 35°N and 75°N, where crustal magnetic field signatures could be detected, is largely covered by a series of four quadrangle geological maps at 1:3M-scale (Galluzzi et al., 2016; Guzzetta et al., 2017; Mancinelli et al., 2016; Wright et al., 2019) that Hood et al. (2018) used to locate regions of interest where magnetic anomalies overlap geological features. The strongest magnetic anomalies are found over the Caloris impact region, both inside Caloris Planitia and over the circum-Caloris smooth plains. The area 90–270°E is

largely biased by Caloris-based anomalies, but the opposite longitudes offer the chance to locate some magnetic anomalies that are correlated with isolated features far from this large basin (Fig. 1). The most significant ones are located at Vyasa crater (275°E; 50°N), the B31 basin (3°E; 36°N; Orgel et al., 2020), the Northern Rise (30°E; 68°N; Zuber et al., 2012), Rustaveli crater (82°E; 52°N), and Stieglitz crater (67°E; 73°N) (Hood et al., 2018; Fig. 1). Vyasa and the B31 basin are very old impact sites, degraded and overlapped by other craters, hence the magnetic anomalies' origins are difficult to interpret. On the other hand, the latter three sites are all located within the young Borealis Planitia characterized by smooth plains, the youngest extensive plains unit on Mercury. These are widespread effusive volcanic plains thought to be as old as 3.7 Ga (Ostrach et al., 2016) and not younger than 3.5 Ga (Byrne et al., 2016). There is no clear evidence on Mercury that effusive volcanism alone brought magnetic carriers to the upper crust. In fact, Borealis Planitia does not show widespread magnetic anomalies (Hood et al., 2018).

Stieglitz and Rustaveli craters, located within Borealis Planitia and away from the localized Northern Rise magnetic anomaly, represent an interesting case study for understanding whether some impactors played a role as suppliers of magnetic carriers to Mercury's crust. Differently from all other features corresponding to the magnetic anomalies listed above, these two young and fresh craters, which still maintain fresh morphologies and are younger than nearby volcanic plains, offer the chance to study their impact dynamics and to relate these to the relative location of their off-center magnetic anomalies. These are the only two craters that permit such a study within the available crustal magnetic field map.

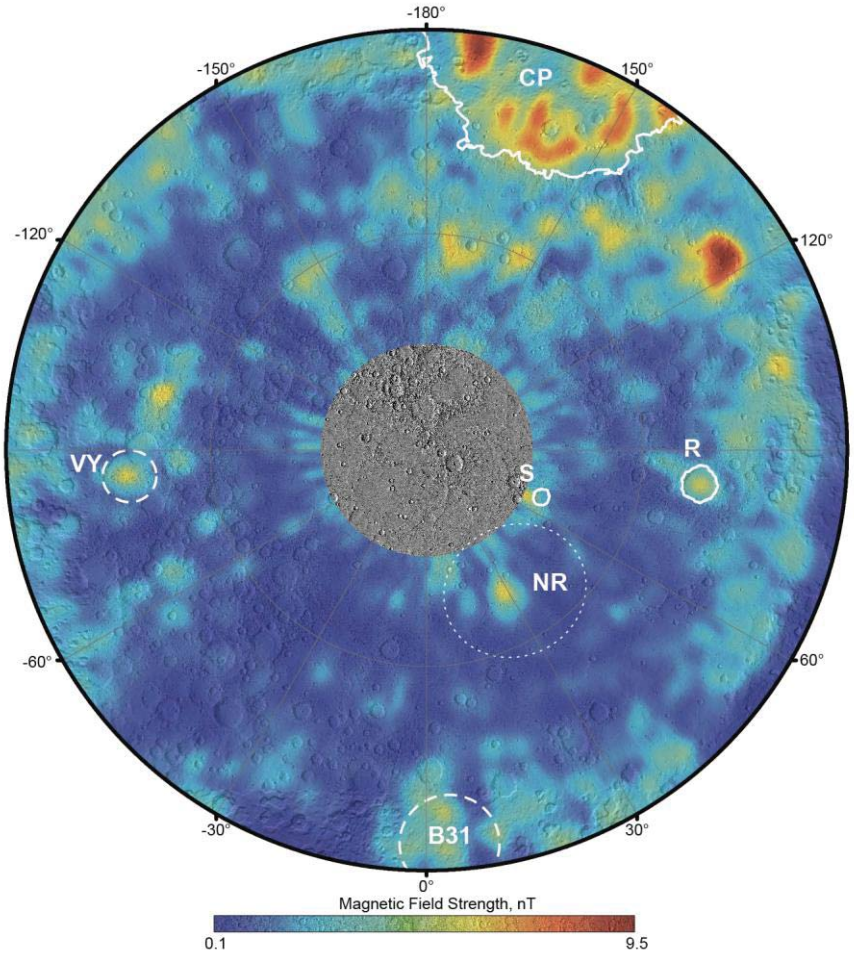

Figure 1. Magnetic field intensity at 40 km altitude (resolution of 1 degree, Hood et al., 2018) superposed on a MLA shaded relief basemap in stereographic north pole projection (from 35°N to 90°N). Major anomalies cited in the text are labelled with letters and the associated feature extent is indicated by outlines. Caloris Planitia (CP), Rustaveli crater (R) and Stieglitz crater (S) are shown with solid white outlines. The ancient basins Vyasa (VY) and B31 basin (B31) are indicated by dashed outlines. The approximate extent of the Northern Rise (NR) is shown with a white dotted outline.

2 Geological Results

We used the MESSENGER Mercury Dual Imaging System (MDIS; Hawkins et al., 2007) basemap datasets and other derived products to map the geomorphology of Stieglitz and Rustaveli craters. For complete information on the datasets and methods used for this analysis see the supporting information (Text S1).

2.1 Stieglitz crater

Stieglitz crater is a mature-complex crater (see morphologic crater classification of Baker et al., 2011, for details) located in Borealis Planitia, just outside the north-eastern limit of the Northern Rise (67.63°E; 72.53°N). Stieglitz has a roughly circular outline with a slight tendency toward polygonality and has a U-shaped central peak with bilateral symmetry (Fig. 2a). It is the youngest crater of its size in its surrounding area (Fig. 2a) and belongs to degradation class c4 in the 5-class system by Kinczyk et al. (2020) and would be classified as a C3 in the 3-class system used by Galluzzi et al. (2016) (note our convention of using 'c' for the 5-class system and 'C' for the 3-class system, where both systems use higher numbers to indicate less degradation). This and its stratigraphic position suggest a Mansurian age (e.g., Wright et al., 2019). Its diameter is ~95 km but increases up to ~105 km in the NW–SE direction apparently mostly because of crater-wall collapses associated with terrace formation. The Mercury Laser Altimeter (MLA; Cavanaugh et al., 2007) north polar Digital Terrain Model (DTM) reveals that the rim is slightly higher in the arc tracing the SW rim than on the opposite side (Fig. 2b).

Overall, a broad degree of radial symmetry can be observed in the continuous ejecta blanket that extends up to ~one crater radius from most of the rim crest, but slightly farther in the SW (Fig. 2c). The crater central peak is at the center of the floor and its U-shape opens towards the SW. A few isolated central peak outliers are located to the NE of the main peak (Fig. 2c). The continuous ejecta includes smooth patches of the kind generally interpreted as melt pools (e.g., Chapman et al., 2018; Wright et al., 2019), which is supported by analogy with lunar examples (e.g., Hawke and Head, 1977). At Stieglitz, these are a few kilometers across and mostly clustered on the northern part of the blanket close outside the crater rim. Some less extensive pools are found WSW of the crater rim (Fig. 2c).

A more pronounced asymmetry is observed by analyzing the secondary crater chains directly associated with the Stieglitz impact (Fig. 2c,d). These extend further in the NW–SE and NE–SW directions, while there is a discernable deficiency of chains at the NNE of the crater, overall showing an axial symmetry in the NNE–SSW direction.

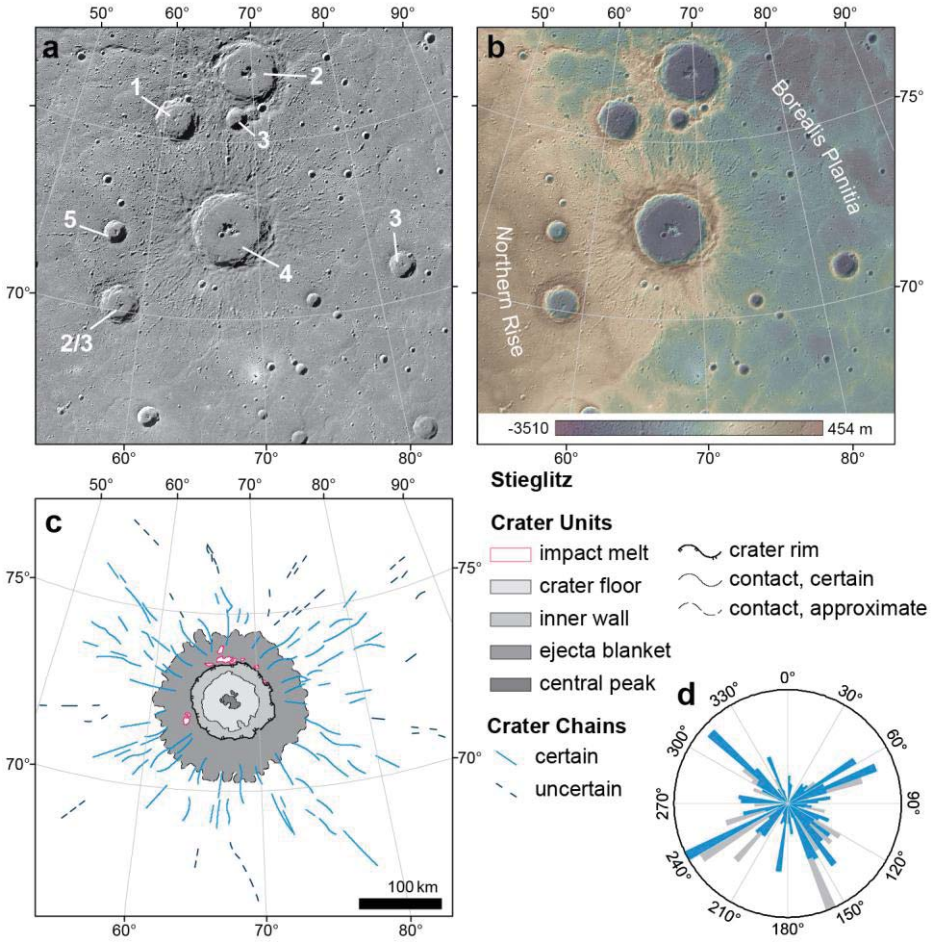

Figure 2. Stieglitz crater in stereographic projection centered on the crater center (67.63°E; 72.53°N): **a**) Relative age of Stieglitz and the surrounding craters from the oldest (1) to the youngest (5) on the HIE basemap at 166 m/pixel; **b**) MLA north-polar DTM; **c**) Simplified geological map showing the trend of certain and uncertain secondary crater chains related to the Stieglitz impact; **d**) Rose diagram analysis of crater chains showing the start and end azimuth of chains indicated by the blue and grey bins, respectively.

2.2 Rustaveli basin

Rustaveli (82.74°E; 52.41°N, Fig. 3a) is a peak-ring basin superposing the smooth plains of Borealis Planitia in the northeast of Mercury's Hokusai quadrangle. Wright et al. (2019) mapped Rustaveli as degradation class c4 in the 5-class system and C3 in the 3-class system. This and its stratigraphic position suggest a Mansurian age (e.g., Wright et al., 2019), as for Stieglitz crater. The crater rim is symmetrical, but slightly higher in its southeastern arc (Fig. 3b), and also somewhat polygonal. A radially textured ejecta blanket (mapped in the same way as for Stieglitz) extends about one crater diameter from the rim at all azimuths (Fig. 3c). Numerous patches of smooth plains are perched in the ejecta proximal to Rustaveli's southeastern rim (Fig.

3c). These smooth patches are probably ponded impact melt that was ejected from the crater cavity during excavation (Wright et al., 2019). Much more extensive smooth plains extend across the whole of Rustaveli's interior, and those materials are sufficiently thick that only the tops of the basin's peak-ring elements are apparent. The volume necessary to achieve this suggests that at least some of the smooth material within Rustaveli was emplaced by post-impact volcanism, overlying any melt produced by the impact. The exposed peak-ring appears somewhat elliptical, with its long-axis oriented east–west (Wright et al., 2016). Our map of secondary crater chains shows a deficiency of chains between W and NW (Fig. 3c,d). Figure 3c also shows a slight deficiency of chains in the southern part, in the region of a pre-existing 50 km diameter crater. We have no explanation of how a pre-existing craters could affect secondary impacts (or secondary crater retention) over such a wide area, so this may be no more than random variation. Because chains are not all exactly radial this local deficiency is not so apparent in Figure 3d, which records direction rather than location.

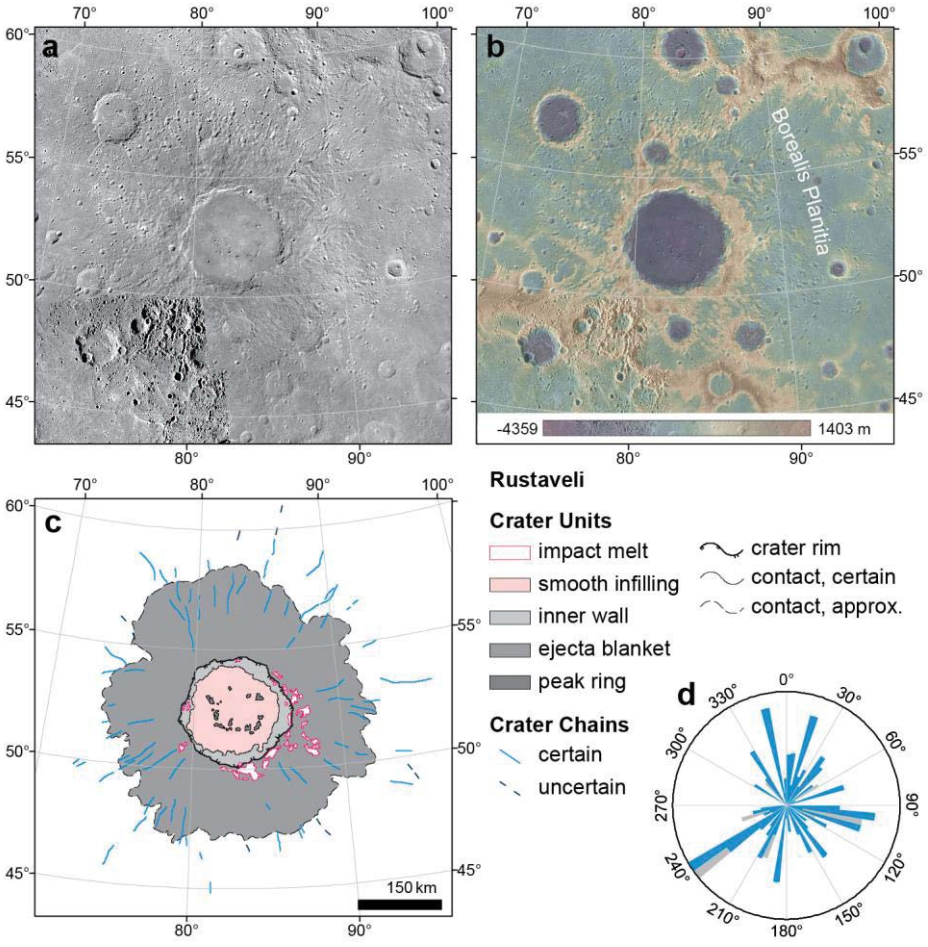

Figure 3. Rustaveli crater in stereographic projection centered on the crater center (82.74°E; 52.41°N): **a**) BDR basemap at 166 m/pixel; **b**) DLR stereo-DTM (west of 90°E) and MLA DTM (east of 90°E); **c**) Simplified geological map (modified from Wright et al., 2019) showing the trend of certain and uncertain secondary crater chains related to the Rustaveli impact; **d**) Rose diagram analysis of crater chains showing the start and end azimuth of chains indicated by the blue and grey bins, respectively.

3 Observable asymmetries and impact dynamics

3.1 Stieglitz crater impact analysis

We consider two possible impact scenarios for Stieglitz fully described in the supporting information (Text S2).

The first one considers the crater's subtle asymmetries as: a) the deficiency of chains radiating towards the NNE (Fig. 2d); b) the NNE-SSW orientation of the symmetry axis of the U-shaped peak (Fig. 2a); c) the highest observable rim topography at S (Fig. 2b); d) the orientation of the symmetry axis of the continuous ejecta blanket in the NNE-SSW direction

(Fig. 2c). Instead, the second scenario considers: a) a wider rim arc toward the N (Fig. 2b); b) the location of most melt pools to the N (Fig. 2c); the location of the deepest secondary crater chain to the N (Fig. S1a, cf. Fig. 2b); the central peak outliers just north of the central peak (Fig. 2c).

By comparison with previous studies and simulations on oblique impacts (Gault and Wedekind, 1978; Schultz, 1992; Pierazzo and Melosh, 2000; Ekholm and Melosh, 2001; Elbeshausen et al., 2009; Kenkmann et al., 2014; Neish et al., 2014) the first scenario results in a probable impactor trajectory from NNE to SSW and impact angle range of 40–50° (Fig. S1a, case 1), while the second one results in a probable impactor trajectory from S to N and impact angle range of 40°–45° (Fig. S1a, case 2). The latter scenario is better constrained than the first one since it takes into account the pre-existing topography (Text S2).

3.2 Rustaveli basin impact analysis

Impact azimuth is less well-constrained for Rustaveli because of its overall morphological symmetry. The peak-ring is too obscured by smooth plains to assess if there is a downrange gap that might indicate impactor azimuth. The crater rim is approximately circular and the rim is higher in the north and east than it is in the southwest, which could imply an impact direction towards the northeast (see Gault and Wedekind, 1978). However, Rustaveli appears to have formed on originally uneven topography (elevated in the southwest and low in the northeast), which could have influenced the evolution of the rim height. Rustaveli's impact ejecta is not obviously asymmetrically distributed, which requires the impact angle to be > 40° above the horizontal, as with Stieglitz. The mapped peak-ring elements appear to form a ring elongated the east-southeast, but no other works have suggested that an elliptical peak-ring is indicative of the impactor azimuth, unless we consider this ellipticity to be due to sense of transport (see Elbeshausen et al., 2009). The strongest asymmetry is the concentration of impact melt in the same direction, just beyond the crater rim. This evidence likely reflects deposition downrange and suggests an impactor travelling from the west-northwest towards the east-southeast with an impact angle of 40–45° (Fig. S1b).

4 Correlation with magnetic anomalies

To analyze the correlation with magnetic anomalies, we superimpose the Hood et al. (2018) crustal magnetic anomalies dataset onto the maps in figures 2c and 3c. We also use the method of Parker (1991; hereafter called Parker's method), a unidirectional magnetization

direction technique that can locate the magnetized material under certain limits (Oliveira et al., 2017). In practice, the strongest dipoles locate the magnetized material and, therefore, the magnetic carriers. If these magnetic carriers are related to the impactor, then some constraints can be made. We also account for acceptable offsets between the strongest dipoles and the geological features possibly due to the gap between the resolution of the basemap (166 m/pixel) and that of the crustal magnetic field map (1 degree at 40 km altitude, i.e. 30 km).

Overall, the most probable impact angle for all planetary bodies is 45° (Gilbert, 1893; Shoemaker, 1962). In the scenarios above, the two analyzed craters are not far from this standard case. Although this impact angle usually produces a general morphological symmetry, if the impactor were constituted (in whole or in part) by magnetic carriers, observable magnetic asymmetries caused by the heterogeneous distribution of the impactor's melt would still be large, as shown in Wieczorek et al. (2012) for the lunar case.

For Stieglitz, the surface with field intensities larger than 3 nT includes most of the ejecta melt locations. The cluster of impact melt ponds to the north of the crater lies on or near the ~5 nT magnetic field strength contour, and the largest strength of ~7 nT nearly corresponds to the deepest secondary chain (Fig. 4a). Although this chain feature is too small and shadowed to reveal whether it hosts ponded melt at the available image resolution and illumination conditions, it is possible that some melt is present within it. This strong magnetic anomaly is fully compatible with the second scenario (see Fig. S1, case 2).

The strongest dipoles given by inversions using Parker's method are distributed in one single cluster toward the north outside the crater rim, next to the crater's deepest secondary chain, adding weight to the hypothesis that this area encompasses magnetic material (Fig. 4b). Other weaker dipoles around the same cluster overlap the northern melt pools suggesting that these could encompass part of the magnetic material also. No dipoles are observable on the melt pools to the west of the crater meaning that either no magnetic carriers are present in this area, or that the volume of melt is much smaller. This supports the northward impact direction scenario, if magnetic carriers from the impactor became mixed with the downrange impact melt only.

Rustaveli is associated with a ~5 nT crustal magnetic anomaly in the 40 km altitude map. In contrast to the case of Stieglitz, this anomaly is centered close the crater's midpoint, slightly offset ~20 km east-southeast (Fig. 4c). This offset is somewhat consistent with the downrange

direction implied by Rustaveli's impact melt and secondary crater chain distribution. However, the strongest part of the magnetic anomaly is located within the crater, away from the visible impact melt deposits beyond the crater rim. If the magnetic anomaly is caused by the impact melt, then it is plausible that the magnetic anomaly is centered within Rustaveli because most of its impact melt was retained within the crater, potentially under a covering of post-impact volcanic smooth plains. This is consistent with the impact being only slightly oblique. Moreover, we have to allow for the Rustaveli impact to have been much more powerful than Stieglitz's, since it has formed a larger basin. This implies a greater volume of impact melt both inside and outside Rustaveli crater.

Observing the distribution of dipoles given by Parker's method, we note that the strongest dipoles are located inside the impact crater rim to the south of the crater's center (Fig. 4d), which is where the magnetic anomaly has its strongest intensity also. We also note that several weaker dipoles are located over the perched impact melt ponds. This is consistent with the inferred downrange direction and with the hypothesis that the strongest magnetic carriers were emplaced within the crater. The lack of strong magnetic fields and dipoles over the ejecta melt pools southeast of the crater indicates that either the impact melt was not so enriched in magnetic carriers as the impact melt within the crater, or the volume of melt is much smaller.

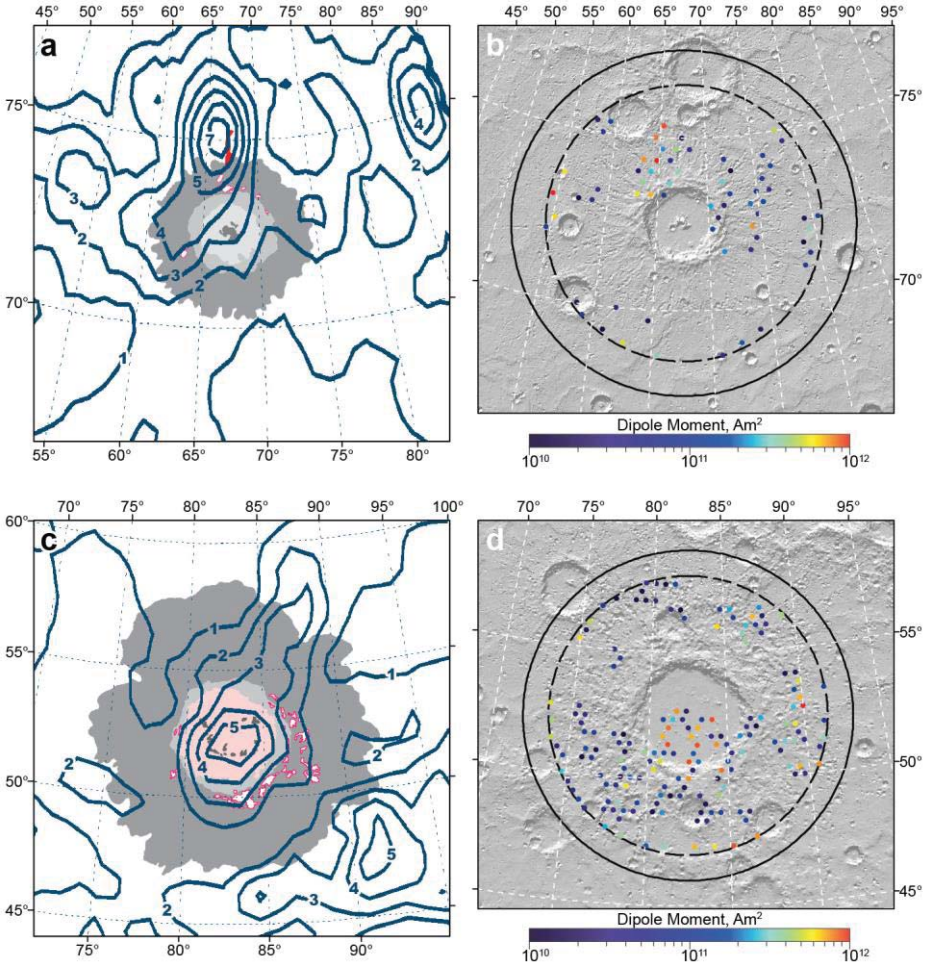

Figure 4. Magnetic anomalies on the analyzed craters. Left and right images use the same projection but with different extents, coordinates are given for comparison: **a**) Magnetic field intensity with 1 nT contours (Hood et al., 2018) on the geological map of Stieglitz. The red polygon indicates the location of Stieglitz's deepest secondary-crater chain; **b**) Inversion dipoles location and intensity on MLA shaded relief for Stieglitz; **c**) Magnetic field intensity with 1 nT contours (Hood et al., 2018) on the geological map of Rustaveli; **d**) Inversion dipoles location and intensity on MLA shaded relief for Rustaveli.

5 Summary and Conclusions

Stieglitz and Rustaveli are two fresh impact craters, younger than the surrounding plains, which still maintain a well-preserved ejecta blanket and visible secondary crater chains. They are characterized by asymmetrical magnetic anomalies possibly correlated with their impact dynamics. Both craters are morphologically symmetrical and impact angles were likely 40–45°. Stieglitz has likely a north downrange direction and Rustaveli a southeast downrange direction. The only clear asymmetry is represented by the locations of impact melt ponds beyond each crater's rim. Photo-interpretative methods support the hypothesis that magnetic carriers were

brought by the impacts. Geological impact analysis shows that the asymmetric magnetic anomalies reported in Hood et al. (2018) correlate well with the locations of the impact melt ponds and the downrange direction. Magnetic field investigation suggests where the magnetized material is supporting the inferred impact direction and the hypothesis that melt is located in the downrange direction. The melt likely recorded, upon quenching, the ambient magnetic field of Mercury at the time of each impact, and it is evidence for an ancient thermo-remanent magnetization. Small signals of some of the mapped pools might not be detectable in MESSENGER data, because they might be too weak or comparable to external magnetic signals at the spacecraft altitude. Further analysis of the impact melt could be done by inferring impact melt volumes that would permit us to convert the magnetic dipoles into an estimate of magnetization (e.g., Hood et al., 2018, Oliveira et al., 2017). However, the available morphological data do not permit us to infer the thickness of the melt pools.

This study represents progress, but our sample is not statistically significant given the large number of craters on Mercury's surface. The number of craters that are related to magnetic anomalies is limited, for which there are two likely explanations. Firstly, because there is no map of the crustal magnetism covering the entire surface of Mercury, given the MESSENGER altitude constraints. Secondly, the magnetic signals might be too weak compared with external magnetic signals over some craters at spacecraft altitudes. This study needs to be further developed using the ESA/JAXA Bepicolombo mission (Benkhoff et al., 2010) datasets. Firstly, BepiColombo will obtain better data for studying Mercury's surface (Rothery et al., 2020) and it will be possible to distinguish smaller pool areas by means of higher resolution imagery (Cremonese et al., 2020). Secondly, it can also help by extending the latitude range over which the crustal magnetic field can be mapped, and by adding other craters/basins to the list of craters related to magnetic anomalies that will complement this study.

Acknowledgments

We thank two anonymous reviewers for improving the manuscript with constructive comments. We acknowledge funding from the Italian Space Agency (ASI) under ASI-INAF agreement 2017-47-H.0. JSO was funded by the ESA Research Fellowship programme in Space Science. JW and DAR were funded by the PLANMAP project during the write-up of this manuscript, which received funding from the European Union's Horizon 2020 research and

314 innovation programme under grant agreement No. 776276. Work at the University of Arizona
315 was supported by grant 80NSSC17K0215 from the NASA Discovery Data Analysis Program.We
316 acknowledge the use of public data from the MESSENGER archive by NASA/Johns Hopkins
317 University Applied Physics Laboratory/Carnegie Institution of Washington. Crustal magnetic
318 field data is available through Hood et al. (2018). A dataset containing the maps that support the
319 findings of this paper can be found in the National Institute of Astrophysics (INAF) repository at
320 http://dx.doi.org/10.20371/INAF/DS/2021_00001.

321

322 **References**

323 Becker, K. J., Robinson, M. S., Becker, T. L., Weller, L. A., Edmundson, K. L., Neumann, G.
324 A., et al. (2016). First global digital elevation model of Mercury. LPI, (1903), 2959.

325 Benkhoff, J., Van Casteren, J., Hayakawa, H., Fujimoto, M., Laakso, H., Novara, et al. (2010).
326 BepiColombo—Comprehensive exploration of Mercury: Mission overview and science
327 goals. Planetary and Space Science, 58(1-2), 2–20.
328 https://doi.org/10.1016/j.pss.2009.09.020

329 Byrne, P. K., Ostrach, L. R., Fassett, C. I., Chapman, C. R., Denevi, B. W., Evans, A. J., et al.
330 (2016). Widespread effusive volcanism on Mercury likely ended by about 3.5 Ga.
331 Geophysical Research Letters, 43, 7408–7416. https://doi.org/10.1002/2016GL069412

332 Cavanaugh, J. F., Smith, J. C., Sun, X., Bartels, A. E., Ramos-Izquierdo, L., Krebs, D. J., et al.
333 (2007). The Mercury Laser Altimeter instrument for the MESSENGER mission. Space
334 Science Reviews, 131(1-4), 451–479. https://doi.org/10.1007/s11214-007-9273-4

335 Chapman, C. R., Baker, D. M., Barnouin, O. S., Fassett, C. I., Marchi, S., Merline, W.J., et al.
336 (2018). Impact cratering on Mercury. In: Solomon et al. (eds.), Mercury: The View after
337 MESSENGER, 217–248, Cambridge University Press.

338 Cremonese, G., Capaccioni, F., Capria, M. T., Doressoundiram, A., Palumbo, P., Vincendon, M.,
339 et al. (2020). SIMBIO-SYS: Scientific Cameras and Spectrometer for the BepiColombo
340 Mission. Space science reviews, 216(5), 1–78.

341 Di Achille, G., Popa, C., Massironi, M., Mazzotta Epifani, E., Zusi, M., Cremonese, G., &
342 Palumbo, P. (2012). Mercury's radius change estimates revisited using MESSENGER
343 data. Icarus, 221(1), 456–460. https://doi.org/10.1016/j.icarus.2012.07.005

344 Elbeshausen, D., Wünnemann, K., & Collins, G. S. (2009). Scaling of oblique impacts in
345 frictional targets: Implications for crater size and formation mechanisms. Icarus, 204(2),
346 716–731. https://doi.org/10.1016/j.icarus.2009.07.018

347 Ekholm, A. G., & Melosh, H. J. (2001). Crater features diagnostic of oblique impacts: The size
348 and position of the central peak. Geophysical Research Letters, 28(4), 623–626.
349 https://doi.org/10.1029/2000GL011989

350 Fegan, E. R., Rothery, D. A., Marchi, S., Massironi, M., Conway, S. J., & Anand, M. (2017).
351 Late movement of basin-edge lobate scarps on Mercury. Icarus, 288, 226–234.

352 Galluzzi, V. (2019). Multi-mapper Projects: Collaborative Mercury Mapping. In H. Hargitai
353 (Ed.), Planetary Cartography and GIS (pp. 207–218). https://doi.org/10.1007/978-3-319-
354 62849-3_9

355 Galluzzi, V., Guzzetta, L., Ferranti, L., Di Achille, G., Rothery, D. A., & Palumbo, P. (2016).
356 Geology of the Victoria quadrangle (H02), Mercury. Journal of Maps, 12, 227–238.
357 https://doi.org/10.1080/17445647.2016.1193777

358 Gault, D. E., & Wedekind, J. A. (1978). Experimental studies of oblique impact. Lunar and
359 Planetary Science Conference Proceedings, 9, 3843–3875.

360 Gilbert, G. K. (1893). The Moon's face: A study of the origin of its features. Philosophical
361 Society of Washington.

362 Guzzetta, L., Galluzzi, V., Ferranti, L., & Palumbo, P. (2017). Geology of the Shakespeare
363 quadrangle (H03), Mercury. Journal of Maps, 13(2), 227–238.
364 https://doi.org/10.1080/17445647.2017.1290556

365 Hawke, B.R. and Head, J.W., 1977. Impact melt on lunar crater rims. In: Impact and explosion
366 cratering: Planetary and terrestrial implications, 815–841.

367 Hawkins, S. E., Boldt, J. D., Darlington, E. H., Espiritu, R., Gold, R. E., Gotwols, B., et al.
368 (2007). The Mercury dual imaging system on the MESSENGER spacecraft. Space
369 Science Reviews, 131(1), 247–338. https://doi.org/10.1007/s11214-007-9266-3

370 Hood, L. L. (2016). Magnetic anomalies concentrated near and within Mercury's impact basins:
371 Early mapping and interpretation. Journal of Geophysical Research: Planets, 121, 1016–
372 1025. https://doi.org/10.1002/2016JE005048

373 Hood, L. L., Oliveira, J. S., Galluzzi, V., & Rothery, D. A. (2018). Investigating Sources of
374 Mercury's Crustal Magnetic Field: Further Mapping of MESSENGER Magnetometer
375 Data. Journal of Geophysical Research: Planets, 123(10), 2647–2666.
376 https://doi.org/10.1029/2018JE005683

377 Izenberg, N. R., Klima, R. L., Murchie, S. L., Blewett, D. T., Holsclaw, G. M., McClintock, et
378 al. (2014). The low-iron, reduced surface of Mercury as seen in spectral reflectance by
379 MESSENGER. Icarus, 228, 364–374. https://doi.org/10.1016/j.icarus.2013.10.023

380 James, P. B. (2018). The Enigma of Mercury's Northern Rise. LPICo, 2047, 6053.

381 Jenness, J. (2014). Polar plots for ArcGIS. Jenness Enterprises. Available at:
382 http://www.jennessent.com/arcgis/polar_plots.htm

383 Johnson, C. L., Phillips, R. J., Purucker, M. E., Anderson, B. J., Byrne, P. K., Denevi, B. W., et
384 al. (2015). Low-altitude magnetic field measurements by MESSENGER reveal
385 Mercury's ancient crustal field. Science, 348, 892–895.
386 https://doi.org/10.1126/science.aaa8720

387 Kenkmann, T., Poelchau, M. H., & Wulf, G. (2014). Structural geology of impact craters.
388 Journal of Structural Geology, 62, 156–182. https://doi.org/10.1016/j.jsg.2014.01.015

389 Kinczyk, M. J., Prockter, L. M., Byrne, P. K., Denevi, B. W., Ostrach, L. R., & Skinner, J. A.
390 (2018). A Global Geological Map of Mercury. Mercury: Current and Future Science of
391 the Innermost Planet.

Kinczyk, M. J., Prockter, L. M., Byrne, P. K., Susorney, H. C. M., & Chapman, C. R. (2020). A morphological evaluation of crater degradation on Mercury: Revisiting crater classification with MESSENGER data. Icarus, 341, 113637. https://doi.org/10.1016/j.icarus.2020.113637

Mancinelli, P., Minelli, F., Pauselli, C., & Federico, C. (2016). Geology of the Raditladi quadrangle, Mercury (H04). Journal of Maps, 12, 190–202. https://doi.org/10.1080/17445647.2016.1191384

Neish, C. D., Madden, J., Carter, L. M., Hawke, B. R., Giguere, T., Bray, V. J., et al. (2014). Global distribution of lunar impact melt flows. Icarus, 239, 105–117. https://doi.org/10.1016/j.icarus.2014.05.049

Oliveira, J. S., Hood, L. L., & Langlais, B. (2019). Constraining the Early History of Mercury and Its Core Dynamo by Studying the Crustal Magnetic Field. Journal of Geophysical Research: Planets, 124(9), 2382–2396. https://doi.org/10.1029/2019JE005938

Oliveira, J. S., Wieczorek, M. A., and Kletetschka, G. (2017). Iron abundances in lunar impact basin melt sheets from orbital magnetic field data. Journal of Geophysical Research: Planets, 122. https://doi.org/10.1002/2017JE005397

Orgel, C., Fassett, C. I., Michael, G., Riedel, C., van der Bogert, C. H., & Hiesinger, H. (2020). Re-examination of the population, stratigraphy, and sequence of mercurian basins: Implications for Mercury's early impact history and comparison with the Moon. Journal of Geophysical Research: Planets.

Ostrach, LK. R., Mest, S. C., Prockter, L. M., Petro, N. E., Byrne, P. K., Finalizing the geologic map of the Borealis quadrangle (H-1) on Mercury, Lunar and Planetary Science Conference, 51, 1121.

Parker, R. L. (1991). A theory of ideal bodies for seamount magnetism. Journal of Geophysical Research, 96(B10), 16101. https://doi.org/10.1029/91JB01497

Pierazzo, E., & Melosh, H. J. (2000). Understanding Oblique Impacts from Experiments, Observations, and Modeling. Annual Review of Earth and Planetary Sciences, 28, 141–167.

Shoemaker, E. M. (1962). Interpretation of lunar craters. Physics and Astronomy of the Moon, 283-359.

Richmond, N. C., and L. L. Hood (2008). A preliminary global map of the vector lunar crustal magnetic field based on Lunar Prospector magnetometer data, J. Geophys. Res., 113, E02010, doi:10.1029/2007JE002933.

Rothery, B., Massironi, M., Alemanno, G., Barraud, O., Besse, S., Bott, N., et al. (2020). Rationale for BepiColombo Studies of Mercury's Surface and Composition. Space Sci Rev, 216, 66. https://doi.org/10.1007/s11214-020-00694-7

Stark, A., Preusker, F., Oberst, J., Matz, K. D., Gwinner, K., & Roatsch, T. (2017). High-Resolution Topography from MESSENGER Orbital Stereo Imaging—The H5 Quadrangle" Hokusai". LPI, (1964), 2287.

Thomas, R. J., & Rothery, D. A. (2019). Volcanism on Mercury, Elements, 15, 27–32. https://doi.org/10.2138/gselements.15.1.27

Tsunakawa, H., Takahashi, F., Shimizu, H., Shibuya, H., & Matsushima, M. (2015). Surface vector mapping of magnetic anomalies over the Moon using Kaguya and Lunar Prospector observations. Journal of Geophysical Research: Planets, 120(6), 1160–1185. https://doi.org/10.1002/2014JE004785

Weider, S. Z., Nittler, L. R., Starr, R. D., McCoy, T. J., & Solomon, S. C. (2014). Variations in the abundance of iron on Mercury's surface from MESSENGER X-Ray Spectrometer observations. Icarus, 235, 170–186. https://doi.org/10.1016/j.icarus.2014.03.002

Wieczorek, M. A., Weiss, B. P., & Stewart, S. T. (2012). An Impactor Origin for Lunar Magnetic Anomalies. Science, 335(6073), 1212–1215. https://doi.org/10.1126/science.1214773

Wright, J., Rothery, D. A., Balme, M. R., & Conway, S. J. (2019). Geology of the Hokusai quadrangle (H05), Mercury. Journal of Maps, 15(2), 509–520. https://doi.org/10.1080/17445647.2019.1625821

Zuber, M. T., Smith, D. E., Phillips, R. J., Solomon, S. C., Neumann, G. A., Hauck, S. A., et al. (2012). Topography of the Northern Hemisphere of Mercury from MESSENGER Laser Altimetry. Science (New York, N.Y.), 217(March), 217–220. https://doi.org/10.1126/science.1218805

Figure 1.

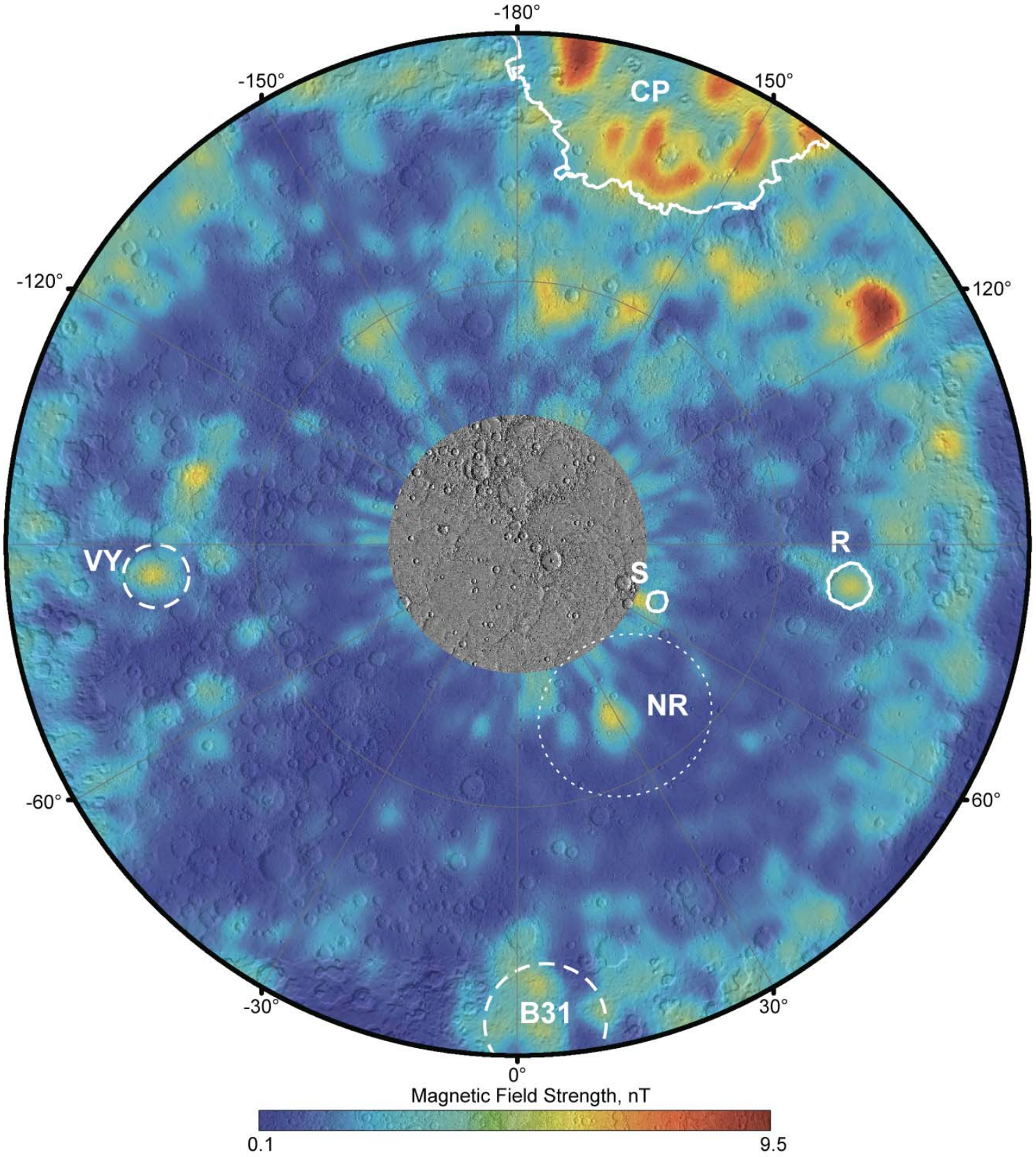
-180°
-150°
150°
-120°
120°
-60°
60°
-30°
30°
0°
CP
VY
S
R
NR
B31
Magnetic Field Strength, nT
0.1
9.5

Figure 2.

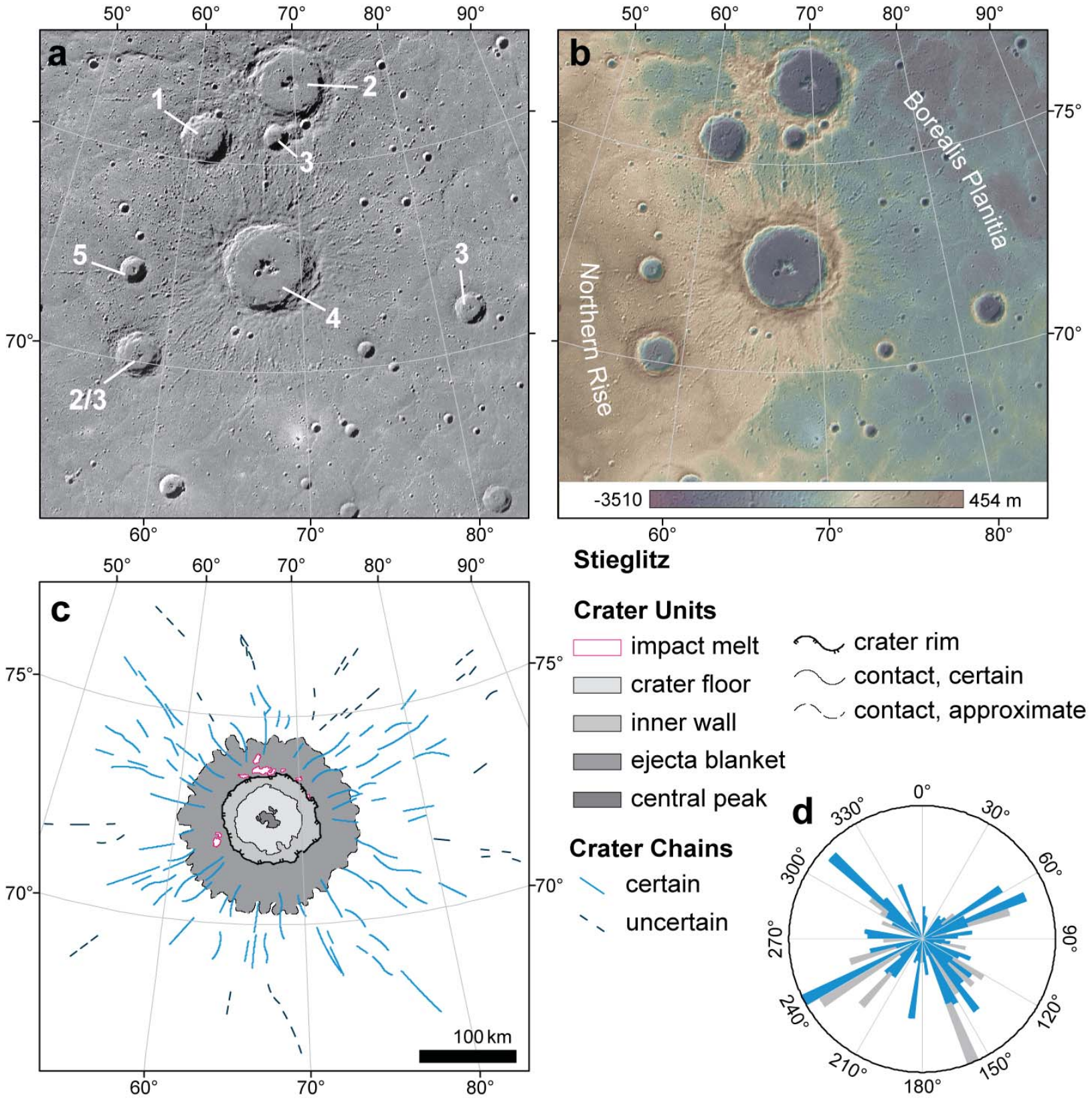
a
b
c
d
50°
60°
70°
80°
90°
75°
70°
1
2
3
4
5
2/3
Borealis Planitia
Northern Rise
-3510
454 m
Stieglitz
Crater Units
impact melt
crater floor
inner wall
ejecta blanket
central peak
crater rim
contact, certain
contact, approximate
Crater Chains
certain
uncertain
100 km
0°
30°
60°
90°
120°
150°
180°
210°
240°
270°
300°
330°

Figure 3.

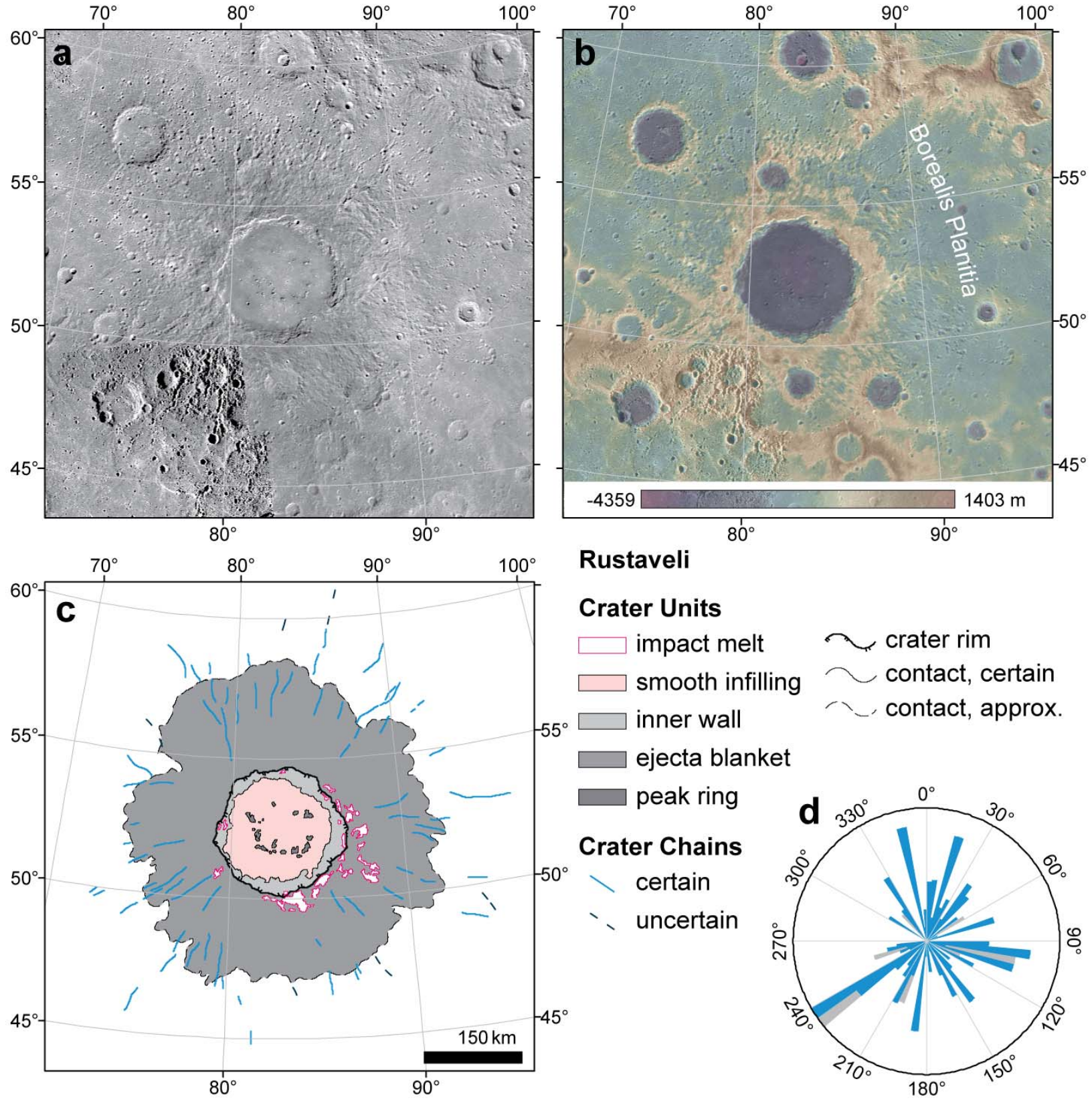
a
b
c
d
70°
80°
90°
100°
60°
55°
50°
45°
Borealis Planitia
-4359
1403 m
Rustaveli
Crater Units
impact melt
smooth infilling
inner wall
ejecta blanket
peak ring
crater rim
contact, certain
contact, approx.
Crater Chains
certain
uncertain
150 km
0°
30°
60°
90°
120°
150°
180°
210°
240°
270°
300°
330°

Figure 4.

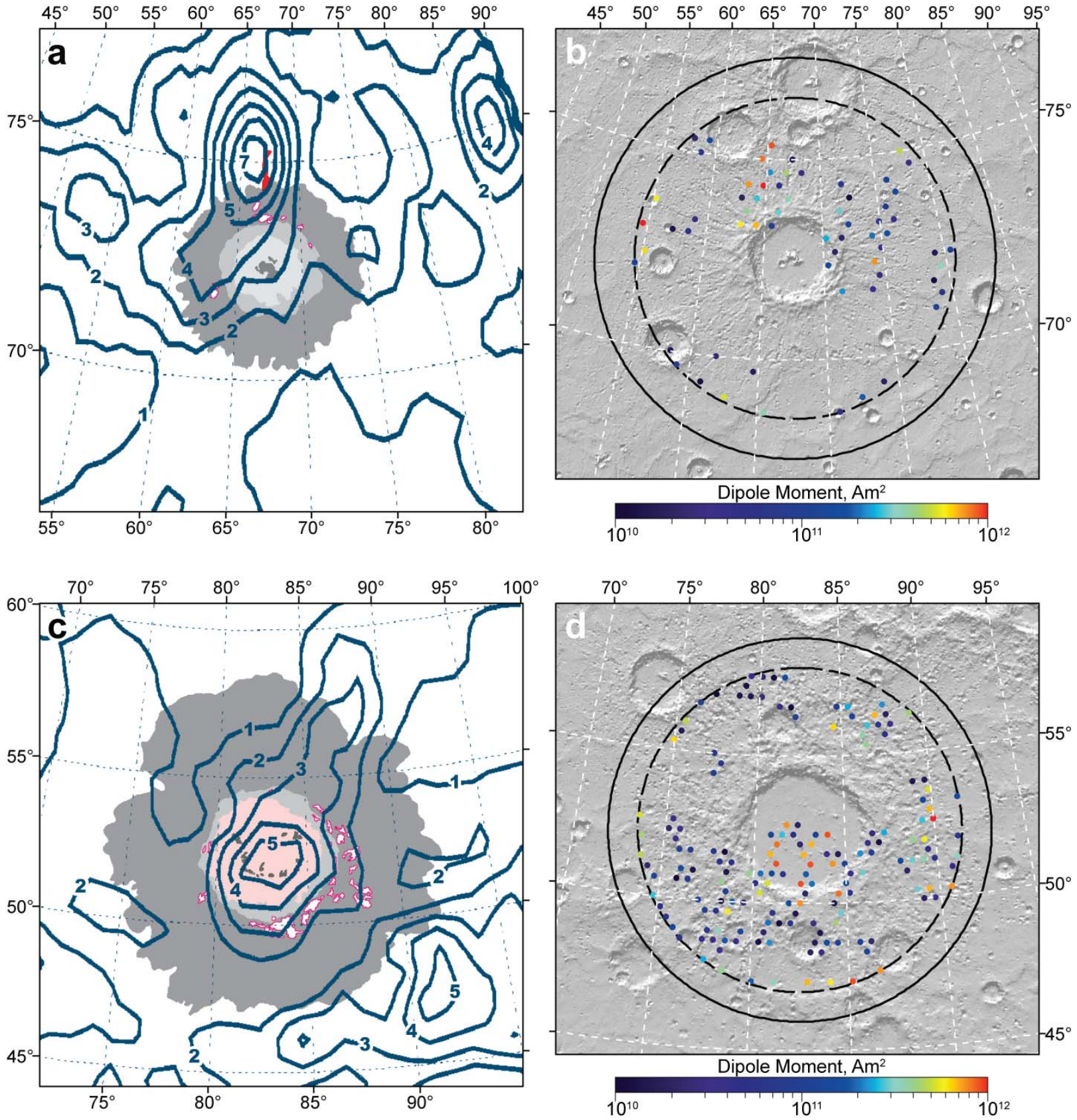
a
b
c
d
45° 50° 55° 60° 65° 70° 75° 80° 85° 90° 95°
75°
70°
55°
60°
65°
70°
75°
80°
1
2
3
4
5
7
Dipole Moment, Am²
10¹⁰
10¹¹
10¹²
70° 75° 80° 85° 90° 95° 100°
60°
55°
50°
45°